# A Tendon-Driven Continuum Manipulator With Robust Shape Estimation by Multiple IMUs

Rui Peng ⬤, Yu Wang ⬤, and Peng Lu ⬤, *Member, IEEE*

*Abstract*—In this letter, a tendon-driven continuum robotic manipulator with three individual continuum sections is developed and manufactured. The main contribution is that we propose a robust and accurate shape estimation method based on the fusion of multi-IMUs for the manipulator, under the PCC (Piecewise Constant Curvature) assumption. To intuitively present the robot's configuration space, we develop a visualization environment to showcase the real-time continuum shape. To validate the proposed system with the estimation method, we evaluate fundamental attributes such as the bending range, tip velocity, effective workspace, and durability. Furthermore, we conduct motion experiments of shape deformation, dynamic tracking, and disturbance resisting. The results show that our proposed estimation method is evaluated to achieve less than 20 mm RMSE on tip motion, during consecutive 3D motions. Meanwhile, we compare the proposed system with previous continuum robotic systems in mechanism properties. Our proposed robotic system has a more compact and efficient structure.

*Index Terms*—Multi-IMUs, tendon-driven continuum robots, and shape estimation.

## I. INTRODUCTION

RECENTLY, continuum or soft robots [1], [2], [3] have raised enormous research interests in the robotics field. Although dexterity is their most significant advantage, it is challenging to build a robust and accurate kinematic model due to numerous mechanical designs, variable loadings, unexpected disturbance, etc. For a continuum manipulator [4], [5], its kinematic model is directly derived from its corresponding continuum shape, with the assumption of PCC (Piecewise Constant Curvature). Unlike discrete rigid-link manipulators, continuum robots' material and actuation approaches are considerably distinctive.

A flexible manipulator [6] formed of connected continuum kinematic modules (CKMs) is presented to ease the fabrication of a continuum robot with multiple degrees of freedom. To overcome the limitations of both borescopes and

continuum robots, a modular design [7] is proposed at their intersection, with both active tendon-driven and passively flexible segments. [8] presents a general framework for the dynamic analysis of tendon-driven co-manipulative continuum robots with flexible objects. Cosserat rod theory for efficient modeling performance [9], and Euler curves are alternatives for modeling continuum robots [10]. Aiming at solving the problems of low flexibility, poor internal extension, low stiffness, and complex motion modes, continuum robots are developed to be more dexterous and capable of switching stiffness [11], [12], [13]. Even though these research works propose different continuum manipulators with well-evaluated modeling approaches, their models are geometrically based on actuating tendon lengths that are vulnerable to unknown payload [14] or disturbance.

To achieve precise and real-time pose solutions of continuum robots, sensor-engaged methods have been investigated recently. A permanent magnetic tracking technology is proposed to track the poses of multiple end effectors of a multi-arm continuum robot [15]. With the aid of image sensors [16], learning-based methods [17], and internal sensors [18], continuum or soft robots are capable of estimating real-time configuration shapes [19] in situations of various tasks, dynamic or constraint workspace. Moreover, multiple inertial measurement units (IMUs) endow a continuum robot with high-frequent orientation feedback on the continuum torso, so that IMU-based continuum kinemactic models could be established [20], [21], [22], [23], [24], [25], [26]. However, these works lack experimental evaluation of shape estimation during continuous locomotion and variable loadings.

To address the above issues, we develop and manufacture a tendon-driven continuum manipulator with three individual continuum sections, as shown in Fig. 1(a). Each section consists of an IMU, several spacer disks, a flexible backbone, four tendons, and origami shell units. By the compact design, the volume of the manipulator's actuation system is limited to $18\%$ of the volume of the whole robotic system. The main contribution is that we propose a multiple IMUs-based shape estimation method, which builds a robust, accurate, and real-time kinematic model for the proposed manipulator. To visualize and monitor the configuration shape simultaneously, we develop a simulative environment as shown in Fig. 1(b). To validate the proposed robotic system and the shape estimation method, we design and conduct solid experiments of shape deformation, dynamic tracking motion, loading tests, disturbance-resistance tests, and system durability tests. We evaluate the estimation accuracy by the root mean square error (RMSE) of the end-effector during numerous tip locomotion. With the novel mechanical and hardware systematic design, the kinematic model derived from the proposed shape estimation method enables the continuum
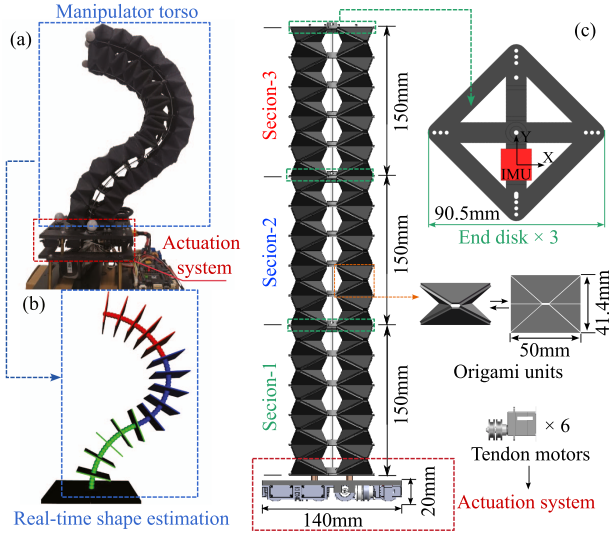
Fig. 1. (a) The authors develop the original prototype of a continuum manipulator with three continuum sections. (b) A virtual robot model based on the proposed shape estimation method is shown in the ROS-Rviz environment. (c) Mechanism details of the proposed continuum manipulator, including the torso, the end disks with IMUs, the actuation system with tendon motors, and origami units.

TABLE I
MECHANISM PARAMETERS OF THE PROPOSED ROBOT

| Element | Material | Quantity | Mass | Core size |
|---------|----------|----------|------|-----------|
| Backbone | Ni-Ti alloy | 1 | 2.0 g | radius: 0.6 mm |
| Mid disk | PLA | 12 | 7.8 g | $64 \times 64 \times 2$ mm |
| End disk | PLA | 3 | 14.2 g | $64 \times 64 \times 7.5$ mm |
| Origami unit | PLA | 60 | 2.7 g | $50 \times 41.4$ mm |
| Tendon | Nylon | 12 | 0.2 g | radius: 0.25 mm |
| IMU | / | 3 | 1.0 g | $15 \times 15 \times 2$ mm |
| Motor | / | 6 | 20.6 g | $23 \times 12 \times 27.5$ mm |

manipulator to implement versatile manipulation tasks in actual applications.

## II. DESIGN AND PRELIMINARIES

### A. System Achitecture

The overall systematic architecture is shown in Fig. 1(c). The torso's total length is 450 mm with three continuum sections, and its diagonal length is 90.5 mm. With an axis-aligned IMU installed on the end disk, every continuum section is driven by two tendon motors (maximum torque: 1 N·m), each of which connects two opposite-rotating tendons. The actuation system which consists of six tendon motors in total, is limited to the size of $140 \times 140 \times 20$ mm³. Moreover, origami units play a role in enclosing the manipulator's torso and connecting two adjacent spacer disks. Detailed mechanics parameters of the proposed system are presented in Table I.

### B. Preliminary Knowledge

According to the system overview, the whole continuum robot is composed of three individual sections. In this letter, each section is complied with the PCC (Piecewise Constant Curvature) assumption. For the continuum manipulator, the generalized coordinate frames are defined as the base frame $\mathcal{B}$ and the end disk frames $\mathcal{E}^i$ ($i \in \{1, 2, 3\}$), shown in Fig. 2(a). Within
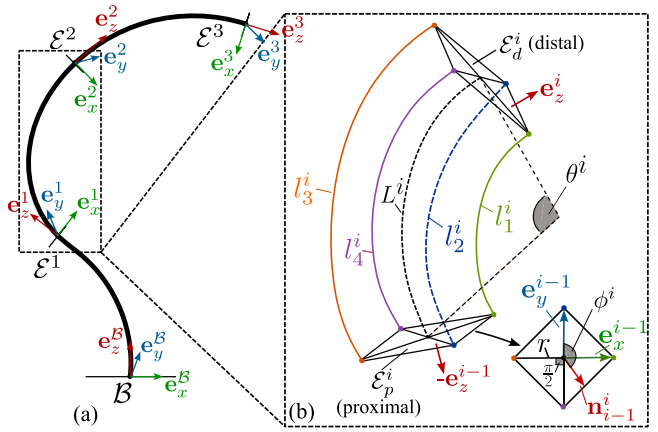


Fig. 2. Configuration space's description of the proposed continuum manipulator. (a) Overview of the whole configuration including key coordinate frames. (b) Single section's configuration including key numerical variables.

TABLE II
NOMENCLATURE IN FIG. 2

| Coordinate frames in Fig. 2 (a) | | PCC-related values in Fig. 2 (b) | |
|---|---|---|---|
| $\mathcal{B}$ | Robot base frame | $\theta^i$ | $i$-th bending angle |
| $\mathcal{E}^i$ | $i$-th end disk frame | $\phi^i$ | $i$-th directional angle |
| $e^{\mathcal{B}}_{x,y,z}$ | Base frame's vectors | $L^i$ | $i$-th arc length |
| $e^i_{x,y,z}$ | End disk frames' vectors | $l^i_{1,2,3,4}$ | $i$-th tendon lengths |

the single section, the geometric relation between the section proximal frame $\mathcal{E}^i_p$ and the section distal frame $\mathcal{E}^i_d$ is presented in Fig. 2(b). An illustration of all the values in Fig. 2 is presented in Table II. As the manipulator's torso is a sequential structure, the current section's distal frame is equivalent to the next section's proximal frame. The generalized state for shape estimation is defined as $\boldsymbol{S}^* = \{\boldsymbol{s}^1, \boldsymbol{s}^2, \boldsymbol{s}^3\}$, including the single section's state $\boldsymbol{s}^i = [\theta^i \phi^i L^i]^\top$: the right upperscript $i \in \{1, 2, 3\}$ denoting the $i$-th section, $\theta^i$ denoting the bending angle, $\phi^i$ denoting the directional angle, and $L^i$ being the constant section's arc length. Formed by four tendons lengths $[l^i_1 l^i_2 l^i_3 l^i_4]^\top$ which are directly obtained by tendon motors, the $i$-th section establishes its geometric configuration:

$$l^i_n = L^i - \theta^i r \cos\left(\phi^i + (n-1) \cdot \frac{\pi}{2}\right)$$

$$\theta^i = \frac{\sqrt{(L^i - l^i_1)^2 + (L^i - l^i_2)^2}}{r}$$

$$\phi^i = -\arctan\left(\frac{L^i - l^i_2}{L^i - l^i_1}\right) \tag{1}$$

where $n \in \{1, 2, 3, 4\}$ denotes the $n$-th tendon, and $r$ denotes the cross-sectional radius of the section. The geometric-config method is regarded as the conventional ("Conv") method for comparison in Section IV.

## III. METHODOLOGY

The shape estimation relying on multiple IMUs is summarized as follows: 1) The quaternion of each IMU is obtained by a lightweight EKF by fusing its acceleration and angular velocity; 2) The updated quaternion is transformed to the rotation matrix, which is used to obtain the normal vector of the IMU plane with respect to the base frame; 3) The included angle between the

proximal disk's normal vector and the distal disk's normal vector is defined as the estimated bending angle $\theta^i$, and the projection vector of the distal disk's normal vector in the proximal plane is utilized to compute the directional angle $\phi^i$. 4) With the constant section's arc lengths, the forward kinematics could be derived to obtain the pose of the end-effector with respect to the base frame.

### A. IMU Orientation Estimation

As shown in Fig. 1, each section is equipped with an IMU on its distal disk. The 6-axis IMU (inertial measurement units) provides measurements of 3-axis acceleration and 3-axis angular velocity, which can be fused by an extended Kalman Filter (EKF) to robustly estimate the orientation of the section's distal disk. The 3-axis angular velocity of the IMU body frame is modeled as:

$$\boldsymbol{\omega}_m = \hat{\boldsymbol{\omega}} + \boldsymbol{b}_\omega + \boldsymbol{\mu}_\omega \tag{2}$$

where $\boldsymbol{\omega}_m$ is the measured angular velocity and $\hat{\boldsymbol{\omega}}$ is the actual angular velocity. $\boldsymbol{b}_\omega$ is random measurement bias and $\boldsymbol{\mu}_\omega$ is zero-mean Gaussian white noise. The 3-axis acceleration of the IMU body frame is modeled as:

$$\boldsymbol{\alpha}_m = \hat{\boldsymbol{R}}(\hat{\boldsymbol{\alpha}} - \boldsymbol{g}) + \boldsymbol{b}_\alpha + \boldsymbol{\mu}_\alpha \tag{3}$$

Also, $\boldsymbol{\alpha}_m$ represents the measured acceleration and $\hat{\boldsymbol{\alpha}}$ denotes actual acceleration in the inertial frame. $\boldsymbol{b}_\alpha$ is random measurement bias and $\boldsymbol{\mu}_\alpha$ is zero-mean Gaussian white noise. $\hat{\boldsymbol{R}}$ denotes the orientation of the IMU with respect to the inertial frame. $\boldsymbol{g}$ is the gravity acceleration.

To derive the EKF, the first step is to initialize the initial quaternion $\boldsymbol{q}_{1|0}^-$ by static measured acceleration, the covariance error matrix $\boldsymbol{P}$ of the IMU quaternion estimation, the covariance error matrix of process noise and measurement noise being $\boldsymbol{U}$ and $\boldsymbol{V}$, respectively. The constant sampling interval is denoted as $\Delta t = 0.001\,s$ and $k$ is considered as the discrete time during the fusion process. The quaternion state transition equation is given as:

$$\boldsymbol{q}_{k|k-1}^- = \left(\boldsymbol{I}_{4\times4} + \frac{1}{2}\boldsymbol{\Omega}_{k-1}\Delta t\right) \cdot \hat{\boldsymbol{q}}_{k-1} \tag{4}$$

where $\boldsymbol{\Omega}_{k-1} = \begin{bmatrix} 0 & -\omega_x & -\omega_y & -\omega_z \\ \omega_x & 0 & \omega_z & -\omega_y \\ \omega_y & -\omega_z & 0 & \omega_x \\ \omega_z & \omega_y & -\omega_x & 0 \end{bmatrix}$, the angular velocity measurement of the IMU is denoted by $\boldsymbol{\omega}_m = [\omega_x \omega_y \omega_z]^\top$ in (2), the prior estimate at time $k$ is denoted as $\boldsymbol{q}_{k|k-1}^- = [q_w q_x q_y q_z]^\top$, and $\hat{\boldsymbol{q}}_{k-1}$ denotes the last quaternion estimate. Thus, the prior rotation matrix $\boldsymbol{R}_k^-$ at time $k$ by $\boldsymbol{q}_{k|k-1}^-$ is denoted as:

$$\boldsymbol{R}_k^- =$$

$$\begin{bmatrix} q_w^2 + q_x^2 - q_y^2 - q_z^2 & 2q_xq_y - 2q_wq_z & 2q_xq_z + 2q_wq_y \\ 2q_xq_y + 2q_wq_z & q_w^2 - q_x^2 + q_y^2 - q_z^2 & 2q_yq_z - 2q_wq_x \\ 2q_xq_z - 2q_wq_y & 2q_yq_z + 2q_wq_x & q_w^2 - q_x^2 - q_y^2 + q_z^2 \end{bmatrix} \tag{5}$$

Then, the updated post-covariance error matrix $\boldsymbol{P}_{k|k-1}^-$ at time $k$ is given as:

$$\boldsymbol{P}_{k|k-1}^- = \boldsymbol{A}_{k-1}\boldsymbol{P}_{k-1}\boldsymbol{A}_{k-1}^\top + \boldsymbol{U} \tag{6}$$

---

**Algorithm 1:** State estimation of an IMU.

1: **Initialization:**
2: $\boldsymbol{q}_{1|0}^- \leftarrow \hat{\boldsymbol{q}}_0$, $\boldsymbol{P}_{1|0} \leftarrow diag(\boldsymbol{I}_4 \times 10^{-3})$
3: $\Delta t \leftarrow$ IMU sampling interval, $g \leftarrow 9.81$
4: $\boldsymbol{U} \leftarrow diag(\boldsymbol{I}_4 \times 10^{-2})$, $\boldsymbol{V} \leftarrow diag(\boldsymbol{I}_4 \times 10^4)$
5: **for** $k = 1$ to $N$ **do**
6:    $\boldsymbol{A}_{k-1} \leftarrow \boldsymbol{I}_{4\times4} + \frac{1}{2}\boldsymbol{\Omega}_{k-1}\Delta t$
7:    $\boldsymbol{q}_{k|k-1}^- \leftarrow \boldsymbol{A}_{k-1} \cdot \hat{\boldsymbol{q}}_{k-1}$
8:    $\boldsymbol{P}_{k|k-1}^- \leftarrow \boldsymbol{A}_{k-1}\boldsymbol{P}_{k-1}\boldsymbol{A}_{k-1}^\top + \boldsymbol{U}$
9:    $h(\boldsymbol{q}_{k|k-1}^-) \leftarrow \boldsymbol{R}_k^- \cdot [00g]^\top$, $\boldsymbol{H}_k \leftarrow \frac{\partial h(\boldsymbol{q}_{k|k-1}^-)}{\partial \boldsymbol{q}_{k|k-1}}$
10:   $\boldsymbol{K}_k \leftarrow \boldsymbol{P}_{k|k-1}^-\boldsymbol{H}_k^\top(\boldsymbol{H}_k\boldsymbol{P}_{k|k-1}^-\boldsymbol{H}_k^\top + \boldsymbol{V})^{-1}$
11:   **if** Acceleration measurement is updated **then**
12:     $\hat{\boldsymbol{q}}_k \leftarrow \boldsymbol{q}_{k|k-1}^- + \boldsymbol{K}_k(\boldsymbol{\alpha}_{m,k} - h(\boldsymbol{q}_{k|k-1}^-))$
13:   **end if**
14:   $\boldsymbol{P}_k \leftarrow (\boldsymbol{I}_{4\times4} - \boldsymbol{K}_k\boldsymbol{H}_k)\boldsymbol{P}_{k|k-1}^-$
15: **end for**

---

where the process transition matrix is denoted as $\boldsymbol{A}_{k-1} = \boldsymbol{I}_{4\times4} + \frac{1}{2}\boldsymbol{\Omega}_{k-1}\Delta t$. Also, the estimated static acceleration in the IMU body frame by (3) and (5) is given as:

$$h(\boldsymbol{q}_{k|k-1}^-) = \boldsymbol{R}_k^- \begin{bmatrix} 0 \\ 0 \\ |\boldsymbol{g}| \end{bmatrix} = |\boldsymbol{g}| \begin{bmatrix} 2q_xq_z + 2q_wq_y \\ 2q_wq_x - 2q_yq_z \\ q_w^2 - q_x^2 - q_y^2 + q_z^2 \end{bmatrix} \tag{7}$$

The Jacobian matrix $\boldsymbol{H}_k$ of $h(\boldsymbol{q}_{k|k-1}^-)$ after computing partial derivatives is given as:

$$\boldsymbol{H}_k = \frac{\partial h(\boldsymbol{q}_{k|k-1}^-)}{\partial \boldsymbol{q}_{k|k-1}} = 2|\boldsymbol{g}| \begin{bmatrix} -q_y & q_z & -q_w & q_x \\ q_x & q_w & q_z & q_y \\ q_w & -q_x & -q_y & q_z \end{bmatrix} \tag{8}$$

Then, the Kalman gain $\boldsymbol{K}_k$ could be given as:

$$\boldsymbol{K}_k = \boldsymbol{P}_{k|k-1}^-\boldsymbol{H}_k^\top \left(\boldsymbol{H}_k\boldsymbol{P}_{k|k-1}^-\boldsymbol{H}_k^\top + \boldsymbol{V}\right)^{-1} \tag{9}$$

With the IMU's acceleration measurement $\boldsymbol{\alpha}_{m,k} = [\alpha_x \alpha_y \alpha_z]^\top$ at time $k$, the updated quaternion after acceleration correction, is given as:

$$\hat{\boldsymbol{q}}_k = \boldsymbol{q}_{k|k-1}^- + \boldsymbol{K}_k \left(\boldsymbol{\alpha}_{m,k} - h\left(\boldsymbol{q}_{k|k-1}^-\right)\right) \tag{10}$$

Also, the updated $\boldsymbol{P}_k$ is given as:

$$\boldsymbol{P}_k = (\boldsymbol{I}_{4\times4} - \boldsymbol{K}_k\boldsymbol{H}_k)\boldsymbol{P}_{k|k-1}^- \tag{11}$$

The EKF iteration process is briefly presented in Algorithm. 1. Thereafter, the orientation denoted by the quaternion of all the end disks is obtained.

### B. Multi-IMUs Based Configuration Space

Consequently, the updated rotation matrix $\hat{\boldsymbol{R}}^i$ from the robot base frame $\mathcal{B}$ to the $i$-th IMU frame whose updated quaternion is denoted by $\hat{\boldsymbol{q}}^i$, is computed by the (5). The base frame $\mathcal{B}$ could be represented by three orthogonal unit vectors: $\mathcal{B} = [\boldsymbol{e}_x^\mathcal{B}\boldsymbol{e}_y^\mathcal{B}\boldsymbol{e}_z^\mathcal{B}]^\top$ or $\mathcal{B} = [\boldsymbol{e}_x^0\boldsymbol{e}_y^0\boldsymbol{e}_z^0]^\top$. The $i$-th end disk frame $\mathcal{E}^i$ is also denoted by three orthogonal unit vectors: $\mathcal{E}^i = [\boldsymbol{e}_x^i\boldsymbol{e}_y^i\boldsymbol{e}_z^i]^\top$, as shown in Fig. 2(a). By the rotation measurement of IMUs, the $\mathcal{E}^i$ is given

as:

$$\mathcal{E}^i = \hat{\boldsymbol{R}}^i \cdot \mathcal{B} \tag{12}$$

Therefore, the normal vector $\boldsymbol{e}_z^i$ and the reference vector $\boldsymbol{e}_y^i$ of the $i$-th IMU plane are obtained by $\mathcal{E}^i$. Here, we defined the included angle between the proximal plane's $\boldsymbol{e}_z^{i-1}$ and the distal plane's $\boldsymbol{e}_z^i$ as the estimated bending angle $\hat{\theta}^i$ of the $i$-th section:

$$\hat{\theta}^i = \arccos\left(\frac{\boldsymbol{e}_z^{i-1} \cdot \boldsymbol{e}_z^i}{|\boldsymbol{e}_z^{i-1}| \cdot |\boldsymbol{e}_z^i|}\right) \tag{13}$$

Furthermore, the normal vector $\boldsymbol{e}_z^i$ of the distal IMU plane is projected into the proximal IMU plane as a 2D vector, and the projection vector $\boldsymbol{n}_{i-1}^i$ is computed as:

$$\boldsymbol{n}_{i-1}^i = \left[\frac{\boldsymbol{e}_z^i \cdot \boldsymbol{e}_x^{i-1}}{|\boldsymbol{e}_x^{i-1}|}, \frac{\boldsymbol{e}_z^i \cdot \boldsymbol{e}_y^{i-1}}{|\boldsymbol{e}_y^{i-1}|}\right]^\top \tag{14}$$

Then, with the defined reference vector $\boldsymbol{e}_y^{i-1}$ of the proximal IMU plane, the estimated directional angle $\hat{\phi}^i$ is given by:

$$\hat{\phi}^i = \arccos\left(\frac{\boldsymbol{e}_z^i \cdot \boldsymbol{e}_y^{i-1}}{|\boldsymbol{e}_y^{i-1}|}/|\boldsymbol{n}_{i-1}^i|\right) \tag{15}$$

Thus, we obtain the estimated result of the manipulator configuration space by the fusion of multiple IMU measurements. The accuracy of the result depends on the measurements' noise and the performance of the EKF. Compared with the conventional method based on the tendon lengths (1), our proposed estimation method solely relies on the IMU sensory information which does not suffer internal friction and tendon slacking. Meanwhile, we present the update manipulator's state $\hat{\boldsymbol{S}}^*$ in a visualization environment, where the simulative model's motion is synchronized with the actual manipulator.

## C. Continuum Forward Kinematics

Through the multi-IMUs method, the estimated state $\hat{\boldsymbol{S}}^*$ is updated in real time with the frequency of 1000 Hz. Furthermore, the pose of each section's distal plane could be computed based on $\hat{\boldsymbol{S}}^*$, especially the pose of the end-effector. Still, for the $i$-th section, its rotation matrix from the proximal plane to the distal plane is given as:

$$\boldsymbol{R}_{i-1}^i =$$
$$\begin{bmatrix} c^2(\hat{\phi}^i)c(\hat{\theta}^i L^i) & s(\hat{\phi}^i)c(\hat{\phi}^i)c(\hat{\theta}^i L^i) & -c(\hat{\phi}^i)s(\hat{\theta}^i L^i) \\ s(\hat{\phi}^i)c(\hat{\phi}^i)c(\hat{\theta}^i L^i) & (1-c^2(\hat{\phi}^i))c(\hat{\theta}^i L^i) & -s(\hat{\phi}^i)s(\hat{\theta}^i L^i) \\ c(\hat{\phi}^i)s(\hat{\theta}^i L^i) & s(\hat{\phi}^i)s(\hat{\theta}^i L^i) & c(\hat{\theta}^i L^i) \end{bmatrix} \tag{16}$$

where $c(\cdot)$ and $s(\cdot)$ denote $\cos(\cdot)$ and $\sin(\cdot)$ operations, respectively. Meanwhile, the translation matrix is given as:

$$\boldsymbol{t}_{i-1}^i = \left[c(\hat{\phi}^i)c(\hat{\theta}^i L^i)/\hat{\theta}^i \quad s(\hat{\phi}^i)c(\hat{\theta}^i L^i)/\hat{\theta}^i \quad s(\hat{\theta}^i L^i)/\hat{\theta}^i\right]^\top \tag{17}$$

Considering the base origin as $\boldsymbol{O}_\mathcal{B} = [x_\mathcal{B} \quad y_\mathcal{B} \quad z_\mathcal{B}]^\top$, the $i$-th section's distal origin $\boldsymbol{O}_{\mathcal{E}^i}$ is given as:

$$\begin{bmatrix} \boldsymbol{O}_{\mathcal{E}^i} \\ 1 \end{bmatrix} = \prod_{j=1}^i \begin{bmatrix} \boldsymbol{R}_{j-1}^j & \boldsymbol{t}_{j-1}^j \\ 0 & 1 \end{bmatrix} \cdot \begin{bmatrix} \boldsymbol{O}_\mathcal{B} \\ 1 \end{bmatrix} \tag{18}$$

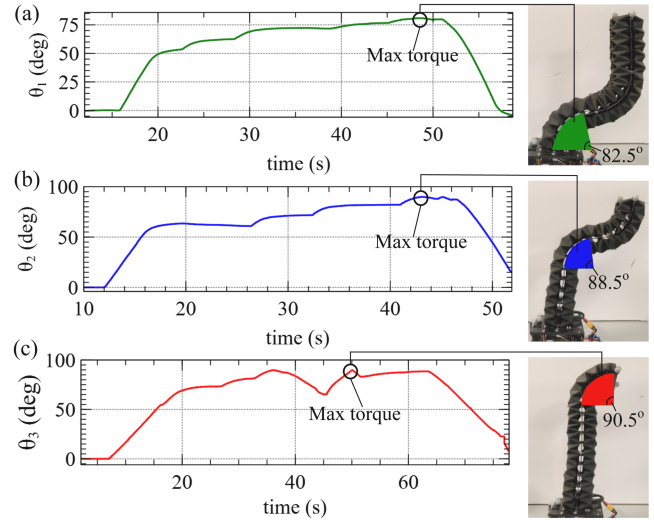

Fig. 3. Maximum bending angles of three sections by the IMUs' EKF, with actual shape situations of the continuum manipulator. (a) The first section: $82.5^o$. (b) The second section: $88.5^o$. (c) The third section: $90.5^o$.

where the $\boldsymbol{O}_{\mathcal{E}^3}$ is considered as the position of the end-effector in the base frame, i.e., the world frame. Therefore, we utilize the mechanism properties including structural parameters and actuation feedback, with the incorporation of embedded attitude sensory information, to achieve real-time and robust shape estimation for the continuum manipulator. The shape estimation results in the corresponding configuration space, which could be transformed into the task space.

## IV. EXPERIMENTS AND RESULTS

### A. Fundamental Attributes Evaluation

As the IMU provides tilting angles of end disks by the EKF, we measure the included angles between two adjacent end disks and obtain the maximum bending angles of all the continuum sections when the related motors reach their maximum torques. As shown in Fig. 3, we record the maximum bending angles and depict the included areas on the manipulator's torso. Thus, the maximum bending angle of the first section is 82.5 °, with 88.5 ° for the second section and 90.5 ° for the third section.

Based on the measured ranges of bending angles, we derive all the effective-reaching points by (18) with all the arbitrary sampled $\theta_1, \theta_2, \theta_3$ and these points build the workspace of the manipulator. Due to the omnidirectional continuum sections, the workspace should be an axisymmetric structure. Thus, we extract the points located at the YOZ plane of the workspace and depict these points in Fig. 4. To reveal the relationship between the manipulator and the workspace, three distinct shapes of the manipulator are presented within the workspace.

To evaluate the motion capability of the continuum manipulator, the tip velocity during manipulation tasks is taken into account. We designed a plane-swing motion with maximum motor torque outputs to make the tip move as fast as possible. Then, we record the linear velocity at every moment and present them in Fig. 5, where we snapshot five shape configurations. It can be noted that the maximum tip velocity is 0.79 m/s.

Moreover, some issues such as tendon slacking, structural deformation, etc., within general continuum robots, because
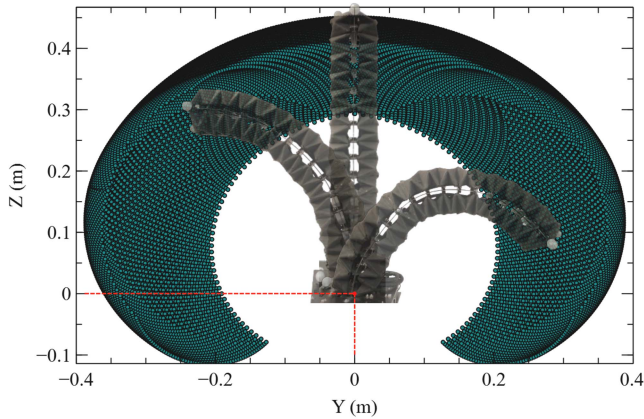
Fig. 4.  Continuum manipulator's workspace in the Y-Z plane by combining effective reaching points of the end-effector, in terms of the maximum bending angles of three sections: $82.5^o$, $88.5^o$, and $90.5^o$.
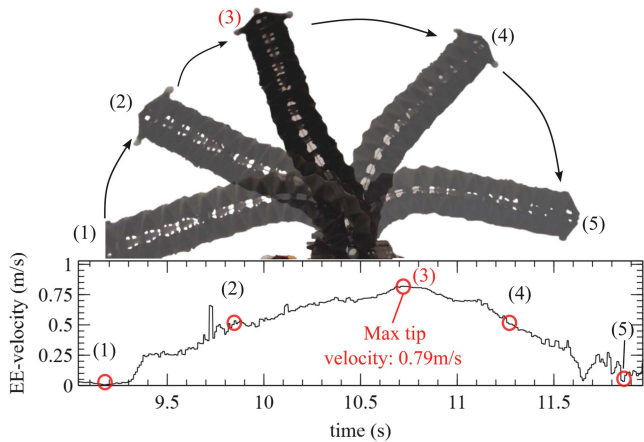


Fig. 5.  Measurement of maximum tip velocity. (1-5) Five shape configurations during the fast swing motion. (3) The maximum tip velocity is 0.79 m/s.

these issues result in frequent damage to the robotic systems. Thus, we designed 20 times of consecutive and same motion experiments without any manual interference and maintenance to verify the system durability of our manipulator. One of the experiments is presented in Fig. 6, with the whole duration being 90 s. With the IMU installed on the EE, we generate a series of desired Roll and Pitch angles for the closed-loop attitude controller. From the experimental plot, the actual Roll and Pitch angles can track the desired commands well with real-time tracking errors of less than 5 °. Also, the position result of the end-effector is derived from our estimation method during the single experiment.

### B. Comparison With Previous CRs

We select several representative continuum robots from the recent literature and focus on the properties of continuum section quantity, the volume ratio of the robot torso to the whole system, the robot torso's total length, the range of the experimental workspace, the tip velocity, the tip accuracy, the tip loading, and the system durability. We list all the corresponding details in the Table III.

It is evident that our system has triple sections and the highest volume ratio of 82.4% within these previous CRs. When the
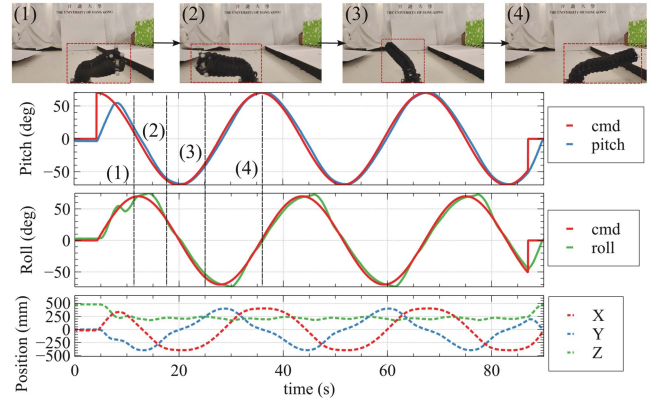


Fig. 6.  System operation durability evaluation of the proposed manipulator by consecutively conducting the closed-loop attitude-tracking motion. The Roll and Pitch angles are derived from the attitude of the end-effector. "cmd" means the input command.

torso length exceeds 400 mm, only ours and Ref [6] have the omnidirectional workspace in experiments. By comparison, our system has sufficient degrees of freedom (DoF) and workspace for achieving dexterous locomotion in 3D space, with a compact mechanical design for optimal system structures. Moreover, thanks to the novel system design, the potential of tendon motors can be facilitated as much as possible: 1) one tendon motor actuates two tendons simultaneously to control "pull" and "push" movements of the associated tendons; 2) the outputs of the tendon motors can be directly transformed into the changes of tendon lengths. Thus, it is more convenient for the proposed manipulator to actuate the tip motions with the high tip velocity (maximum 0.79 m/s in Table III) and without the issue of tendon slacking (high durability: $\geq 1800$ s). Even though the tip accuracy ($\leq 15$ mm) of our work is not as accurate as some works, we evaluate the robustness of our proposed method under variable loadings with a maximum loading of 480 g. Also, the tip accuracy is affected by the mechanism structure and forward kinematics model instead of solely the estimation method.

### C. Comparison With IMUs Based Methods

An inside IMU provides orientation measurements by prevailing EKF for continuum manipulators [20], [21], [22], [23], [24], as shown in Table IV. Even though these works give shape estimation performance on their continuum platforms, we verify our estimation method by high-accurate IMU's orientation estimation, stable tip accuracy under variable loading, consecutive shape-changing motion and trajectory tracking motion in 3D space, and a triple-section continuum manipulator which conducts large-bending motion in the experiments. Our proposed method possesses a more comprehensive evaluation result on our continuum robot platform, which is expected to be implemented in actual applications.

### D. Shape Deformation Evaluation

The fundamental locomotion of the continuum manipulator is the formation of different bending shapes. To present the deformation performance, we design a series of consecutive static shapes for the proposed manipulator to implement. The shape deformation process of the Y-Z plane is shown in Fig. 7 (a, 1-10), with real-time estimated continuum shapes in the

TABLE III
MECHANISM COMPARISON BETWEEN PREVIOUS CRS AND OURS

| CR | Section | Volume ratio | Omnidirectional angle | Torso length | Max tip velocity | Max tip error | Tip loading | Durability |
|---|---|---|---|---|---|---|---|---|
| **Ours** | **Triple** | **82.4%** | **360°** | **450 mm** | **0.79 m/s** | **≤ 15 mm** | **480 g** | **≥ 1800 s** |
| Ref [6] | Triple | 10.4% | 360° | 670 mm | 0.02 m/s | ≤ 7.74 mm | 0 g | ≥ 230 s |
| Ref [14] | Double | ≤ 30% | 180° | 350 mm | / | ≤ 10.12 mm | 80 g | / |
| Ref [18] | Triple | ≤ 10% | 360° | 75 mm | ≤ 0.1 m/s | / | 20 g | 120 s |
| Ref [15] | One | ≤ 5% | 360° | 84 mm | 0.008 m/s | 1.74 mm | 0 g | / |
| Ref [13] | One | ≤ 50% | 90° | ≤ 150 mm | 0.012 m/s | 0.88 mm | 0 g | / |
| Ref [11] | Triple | ≤ 5% | 360° | ≤ 50 mm | / | 2.3 mm | 200 g | / |
| Ref [12] | Triple | ≤ 10% | 180° | 639 mm | ≤ 0.1 m/s | / | 0 g | 70 s |
| Ref [24] | Triple | ≤ 50% | 180° | 525 mm | / | < 38 mm | 0 g | / |
| Ref [5] | Triple | / | 360° | 80 mm - 540 mm | ≤ 0.1 m/s | ≤ 3 mm | ≤ 300 g | 30 s |

TABLE IV
IMUS BASED METHOD COMPARISON

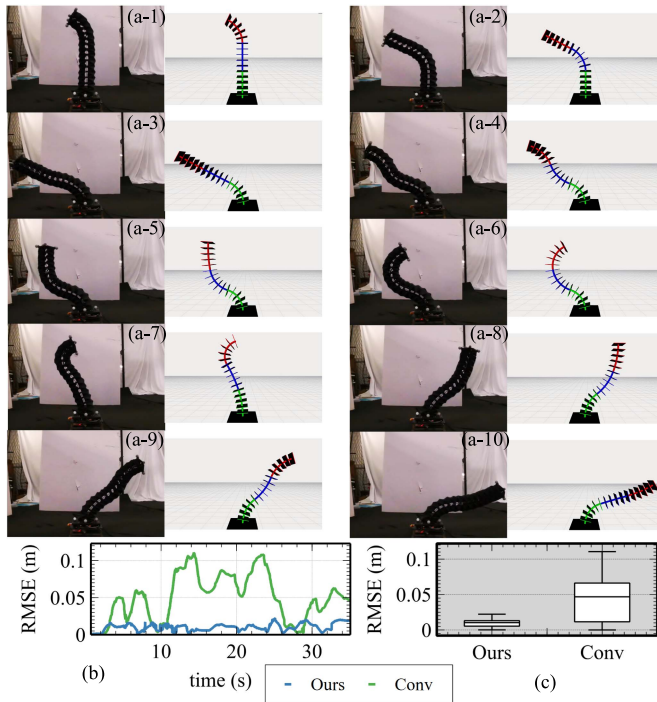| Method | IMU | Loading | Dynamic motion | Section |
|---|---|---|---|---|
| **Ours** | **0.2°** | **80 - 480 g** | **3D & consecutive** | **Triple** |
| Ref [20] | / | / | 3D & discrete | One |
| Ref [21] | / | ≤ 100 g | 3D & consecutive | Double |
| Ref [22] | / | / | 2D & consecutive | Double |
| Ref [23] | 1.1° | / | / | One |
| Ref [24] | / | / | 2D & discrete | Triple |



Fig. 7. (a, 1-10) The shape-changing process with real-time estimated shapes during the motion in the Y-Z plane. (b) Position error results (RMSE) of our method and the conventional method during the motion. (c) RMSE box plot of the motion. "Ours" denotes our shape estimation method and "Conv" means the conventional method.

Moreover, the error distribution of our method and the conventional one during the shape deformation is depicted in a box plot, shown in Fig. 7(c). It can be investigated that the error of our method distributes between 5 mm and 15 mm with a maximum error of 25 mm, while the conventional one's error distributes between 20 mm and 60 mm with a maximum error of 110 mm. Therefore, our method generates more stable estimation results. In the experiment of shape deformation, the error of the end-effector's position evaluates the accuracy of our shape estimation method in a single plane.

### E. Dynamic Tracking Evaluation

To present the dynamic motion performance of the proposed manipulator, we designed six 3D trajectories for the manipulator's tip to track in real time. The trajectories are defined as the trajectory with three waypoints, the trajectory with four waypoints, the circle trajectory, the spiral trajectory, the eight-shape trajectory, and the spark trajectory. We obtain the estimated position derived from our proposed estimation method and the ground truth of the actual tip position. The tracking results are presented in Fig. 8. It can be found that the result of our method (blue curves) tracks the result of the ground truth (red curves) with close convergence. Also, we record the Euclidean error between our method and the ground truth during all the tracking motions. The RMSE of our method is around 20 mm within a 10 mm floating range, while the RMSE of the conventional method is around 60 mm within a 40 mm floating range. Thus, our method performs more accurate and robust shape estimation during 3D motions.

### F. Estimation Robustness Evaluation

Generally, the tendon-driven continuum robot suffers from external disturbances such as unknown payload or force interference. Thereafter, unpredictable errors will be introduced into the shape estimation based on tendon lengths. To evaluate the disturbance-compliant capability of our manipulator with the proposed shape estimation method, we manually apply forces on the proposed manipulator's torso from different directions and locations to observe the shape changes. As shown in Fig. 9, the real-time estimated shapes can be synchronized with the actual manipulator's configurations.

To further evaluate the robustness of the proposed method, we apply five payloads with increasing weights: 80 g, 180 g, 280 g, 380 g, and 480 g on the tip of the static manipulator to verify the performance of our method under variable loadings. To start with, the shape of the manipulator is controlled to be

visualization environment by our proposed shape estimation method. During the shape deformation experiment, we compare the end-effector's position estimation results of our method and the conventional one with the ground truth which is obtained by a motion capture system, and present errors in Fig. 7(b).
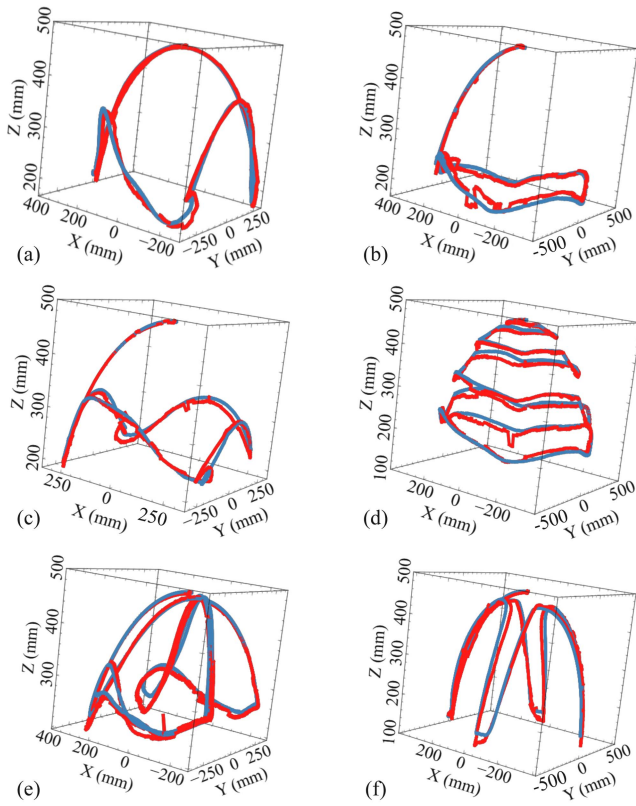
Fig. 8. Tip dynamic tracking results of our method (blue curves). Ground truth (red curves) are obtained by the motion capture system. (a) Trajectory with three waypoints. (b) Trajectory with four waypoints. (c) Circle trajectory. (d) Spiral trajectory. (e) Eight-shape trajectory. (f) Spark trajectory. .
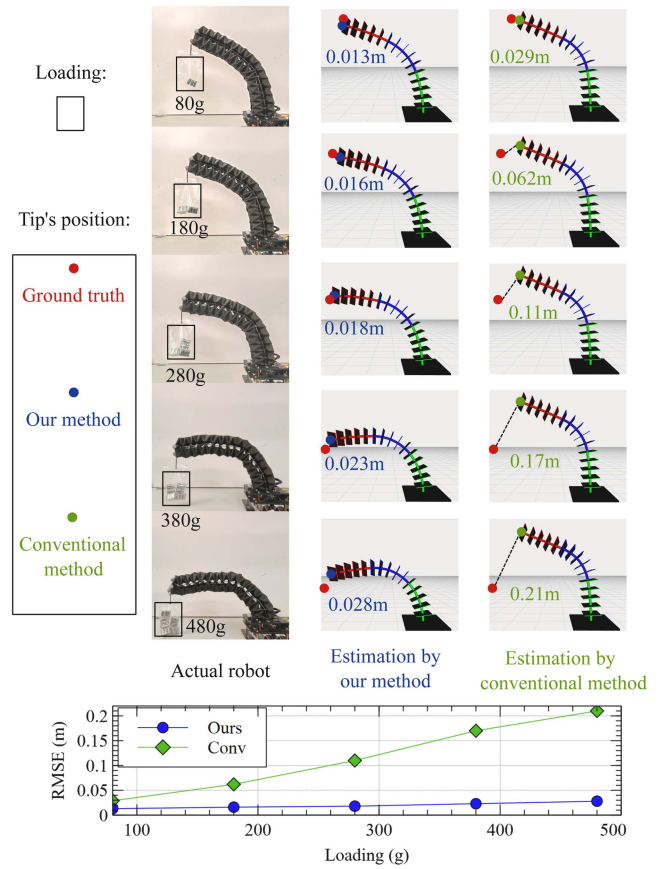


Fig. 9. Shape estimation by the proposed method under external intervention.



Fig. 10. Accuracy evaluation under variable loading (80 g - 480 g). RMSE results of our method and the conventional method are presented.
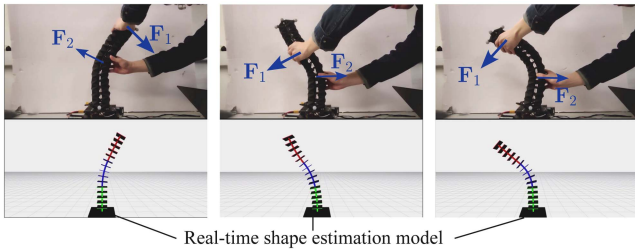


Fig. 11. Dynamic motion with a loading: 200 g. RMSE results of our method ("Ours") and the conventional method ("Conv") are presented.

a curve without any payload. During the whole experiment, the estimated shapes derived from our method and the conventional method are simultaneously visualized. As shown in Fig. 10, the manipulator changes its shape passively with different payloads and the effect is amplified when the payload increases. In the meantime, we compute the tip positions of our method and the conventional one to compare with the ground truth that is obtained by the motion capture system. Also, we visualize the three types of tip positions with current errors. It is evident that our method's tip follows the ground truth closely, while the conventional one's tip remains static because all the tendon motors are locked. According to the relation between errors and payloads, the error of our method increases from 0.013 m to 0.028 m and the conventional one's error increases from 0.029 m to 0.21 m.

After the evaluation of the static robot status with variable loadings, we try to test the performance of our method in
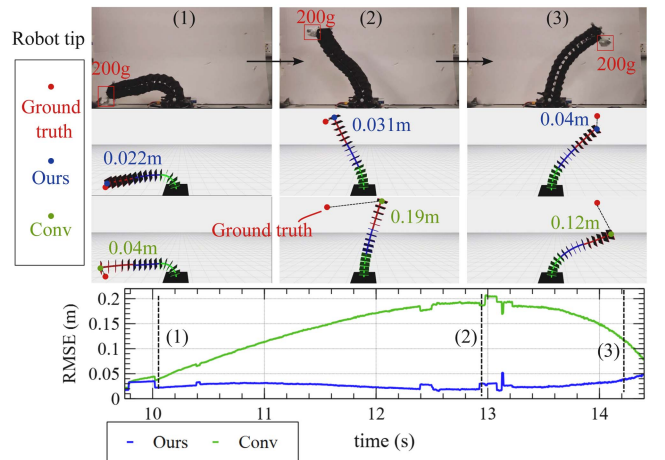
a consecutive motion of the manipulator with a fixed loading, to verify the robustness of our method's dynamic feature. As shown in Fig. 11, we still visualize the estimated models of both two methods with respective errors, compared with the ground truth. During the motion with a loading of 200 g, the error of our method distributes between 0.02 m and 0.04 m, while the conventional one's error floats from 0.04 m to

0.2 m. Thanks to the perceptive modeling for the manipulator's torso by multi-IMUs, our method outperforms the conventional method in the experiments of variable loadings and a movable payload.

## V. Conclusion

In this letter, we propose a tendon-driven continuum manipulator with three continuum sections. The compact mechanical structure reduces the volume of the actuation system significantly to improve the availability rate of the manipulator's torso during manipulation operations. The most vital contribution is to propose a robust shape estimation method based on the fusion of multi-IMUs, thanks to sensitive and reliable sensory measurements. The estimation method further derives the forward kinematic model of the whole system to obtain the pose of the tip. We develop a visualization environment to visualize the real-time estimated shape. The accuracy of the proposed method is proved to be much higher than the conventional tendon-length method during experiments of static and dynamic manipulator motion. Moreover, we evaluate the performance of the method under variable payloads and the estimation stability of the manipulator. It proves that the manipulator can deal with payloads and long-time system performance, which is essential for further advanced algorithm designs and actual manipulation tasks.

## References

[1] R. J. Webster III and B. A. Jones, "Design and kinematic modeling of constant curvature continuum robots: A review," *Int. J. Robot. Res.*, vol. 29, no. 13, pp. 1661–1683, 2010.

[2] M. Russo et al., "Continuum robots: An overview," *Adv. Intell. Syst.*, vol. 5, no. 5, 2023, Art. no. 2200367.

[3] J. Zhang et al., "A survey on design, actuation, modeling, and control of continuum robot," *Cyborg Bionic Syst.*, vol. 2022, 2022, Art. no. 9754697.

[4] R. Peng, Z. Wang, and P. Lu, "AECOM: An aerial continuum manipulator with IMU-based kinematic modeling and tendon-slacking prevention," *IEEE Trans. Syst., Man, Cybern. Syst.*, vol. 53, no. 8, pp. 4740–4752, Aug. 2023.

[5] J. Santoso and C.D. Onal, "An origami continuum robot capable of precise motion through torsionally stiff body and smooth inverse kinematics," *Soft Robot.*, vol. 8, no. 4, pp. 371–386, 2021.

[6] M.-H. Hsu, P.-T. Nguyen, D.-D. Nguyen, and C.-H. Kuo, "Image servo tracking of a flexible manipulator prototype with connected continuum kinematic modules," in *Actuators*, vol. 11, Basel, Switzerland: MDPI, 2022, Art. no. 360.

[7] D. A. Troncoso et al., "A continuum robot for remote applications: From industrial to medical surgery with slender continuum robots," *IEEE Robot. Automat. Mag.*, vol. 30, no. 3, pp. 94–105, Sep. 2023.

[8] A. Jalali and F. Janabi-Sharifi, "Dynamic modeling of tendon-driven co-manipulative continuum robots," *IEEE Robot. Automat. Lett.*, vol. 7, no. 2, pp. 1643–1650, Apr. 2022.

[9] M. Tummers, V. Lebastard, F. Boyer, J. Troccaz, B. Rosa, and M. T. Chikhaoui, "Cosserat rod modeling of continuum robots from Newtonian and Lagrangian perspectives," *IEEE Trans. Robot.*, vol. 39, no. 3, pp. 2360–2378, Jun. 2023.

[10] P. Rao, Q. Peyron, and J. Burgner-Kahrs, "Shape representation and modeling of tendon-driven continuum robots using Euler A Splines," *IEEE Robot. Automat. Lett.*, vol. 7, no. 3, pp. 8114–8121, Jul. 2022.

[11] F. Wang et al., "FIORA: A flexible tendon-driven continuum manipulator for laparoscopic surgery," *IEEE Robot. Automat. Lett.*, vol. 7, no. 2, pp. 1166–1173, Apr. 2022.

[12] D. Shen, Q. Zhang, Y. Han, C. Tu, and X. Wang, "Design and development of a continuum robot with switching-stiffness," *Soft Robot.*, vol. 10, no. 5, pp. 1015–1027, 2023.

[13] Y. Lu, W. Chen, Z. Chen, J. Zhou, and Y.-h. Liu, "FBG-based variable-length estimation for shape sensing of extensible soft robotic manipulators," in *Proc. IEEE/RSJ Int. Conf. Intell. Robots Syst.*, 2022, pp. 01–08.

[14] X. Huang, J. Zou, and G. Gu, "Kinematic modeling and control of variable curvature soft continuum robots," *IEEE/ASME Trans. Mechatron.*, vol. 26, no. 6, pp. 3175–3185, Dec. 2021.

[15] S. Song, H. Ge, J. Wang, and M. Q.-H. Meng, "Real-time multi-object magnetic tracking for multi-arm continuum robots," *IEEE Trans. Instrum. Meas.*, vol. 70, 2021, Art. no. 4008309.

[16] J. Li, F. Zhang, Z. Yang, Z. Jiang, Z. Wang, and H. Liu, "Shape sensing for continuum robots by capturing passive tendon displacements with image sensors," *IEEE Robot. Automat. Lett.*, vol. 7, no. 2, pp. 3130–3137, Apr. 2022.

[17] K. Tanaka, Y. Minami, Y. Tokudome, K. Inoue, Y. Kuniyoshi, and K. Nakajima, "Continuum-body-pose estimation from partial sensor information using recurrent neural networks," *IEEE Robot. Automat. Lett.*, vol. 7, no. 4, pp. 11244–11251, Oct. 2022.

[18] S. Treratanakulchai, E. Franco, A. Garriga-Casanovas, H. Minghao, P. Kassanos, and F. R.Y. Baena, "Development of a 6 DoF soft robotic manipulator with integrated sensing skin," in *Proc. IEEE/RSJ Int. Conf. Intell. Robots Syst.*, 2022, pp. 6944–6951.

[19] D. Kim, M. Park, and Y.-L. Park, "Probabilistic modeling and Bayesian filtering for improved state estimation for soft robots," *IEEE Trans. Robot.*, vol. 37, no. 5, pp. 1728–1741, Oct. 2021.

[20] B. Deutschmann, M. Chalon, J. Reinecke, M. Maier, and C. Ott, "Six-DoF pose estimation for a tendon-driven continuum mechanism without a deformation model," *IEEE Robot. Automat. Lett.*, vol. 4, no. 4, pp. 3425–3432, Oct. 2019.

[21] H. Cheng, H. Xu, H. Shang, X. Wang, H. Liu, and B. Liang, "Orientation to pose: Continuum robots shape reconstruction based on the multi-attitude solving approach," in *Proc. Int. Conf. Robot. Automat.*, 2022, pp. 3203–3209.

[22] M. S. Sofla, M. J. Sadigh, and M. Zareinejad, "Shape estimation of a large workspace continuum manipulator with fusion of inertial sensors," *Mechatronics*, vol. 80, 2021, Art. no. 102684.

[23] K. Stewart, "Robust extended Kalman filter based sensor fusion for soft robot state estimation and control," Ph.D. dissertation, Arizona State University, Tempe, AZ, USA, 2022.

[24] H. Bezawada, C. Woods, and V. Vikas, "Shape reconstruction of soft manipulators using vision and IMU feedback," *IEEE Robot. Automat. Lett.*, vol. 7, no. 4, pp. 9589–9596, Oct. 2022.

[25] Y. J. Martin, D. Bruder, and R. J. Wood, "A proprioceptive method for soft robots using inertial measurement units," in *Proc. IEEE/RSJ Int. Conf. Intell. Robots Syst.*, 2022, pp. 9379–9384.

[26] N. Lin et al., "IMU-based active safe control of a variable stiffness soft actuator," *IEEE Robot. Automat. Lett.*, vol. 4, no. 2, pp. 1247–1254, Apr. 2019.